# Broken symmetry optical transitions in (6,5) single-walled carbon nanotubes containing sp3 defects revealed by first-principles theory

Kasidet Jing Trerayapiwat, $^{\dagger}$  Xinxin Li, $^{\ddagger}$  Xuedan Ma, $^{\ddagger}$  and Sahar Sharifzadeh $^{*,\parallel,\perp,\#,@}$ 

†Department of Chemistry, Boston University, Boston, MA 02215 USA

‡Center for Nanoscale Materials, Argonne National Laboratory, Lemont, IL 60439, USA

¶Consortium for Advanced Science and Engineering, University of Chicago, Chicago,

Illinois, 60637, USA

§Northwestern Argonne Institute of Science and Engineering, Evanston, IL 60208, USA

||Department of Electrical and Computer Engineering, Boston University, Boston, MA

02215, USA

 $\perp Division$  of Materials Science and Engineering, Boston University, Boston, MA 02215, USA

#Department of Physics, Boston University, Boston, MA 02215, USA

@Department of Chemistry, Boston University, Boston, MA 02215, USA

E-mail: ssharifz@bu.edu

### Abstract

We present a first-principles many-body perturbation theory study of nitrophenyl-doped (6,5) single-walled nanotube (SWCNT) to understand how sp3 doping impacts the excitonic properties of the tube. sp3-doped SWCNT comprise a promising class of

optoelectronic materials with bright tunable photoluminescence, long spin coherence, and demonstrated single-photon emission (SPE), motivating the study of spin excitations. We predict that nitrophenyl functional group results in a single unpaired spin localized around the defect site, with associated occupied state at 0.3 eV above the valence band and a spin-split unoccupied state 0.7 eV below the conduction band of the SWCNT. Furthermore, we predict strong excitonic effects, with an exciton binding energy of 1 eV for both pristine and sp3-defective (6,5) SWCNT and multiple low-energy transitions induced by the presence of the defect. By comparing optical absorption and photoluminescence in experiment and theory, we identify the transitions responsible for the red-shifted, defect-induced  $E_{11}^*$  peak, which has demonstrated SPE for some dopants; we find that the presence of this state is due to both the symmetry-breaking associated with the defect and the presence of the defect-induced in-gap state. Furthermore, we find an asymmetry between the contribution of the two spin channels, suggesting this system has potential for spin-selective optical transitions.

Semiconducting single-walled carbon nanotubes (SWCNTs) containing  $sp^3$  quantum defects comprise a promising class of materials for applications in quantum telecommunication and optoelectronics.<sup>1-3</sup> The strong exciton binding within the SWCNT, <sup>4,5</sup> along with exciton trap formation by the defect states, <sup>6,7</sup> lead to a bright, well-resolved photoluminescence (PL) and for some particular defects, room temperature single-photon emission (SPE) with purity of up to 99%.<sup>8-10</sup> In addition, the dephasing time (T2) for a spin localized near the  $sp^3$  defect site can reach the microsecond range, with intrinsic T2 predicted to be in the millisecond range.<sup>11</sup> This high T<sub>2</sub> value coupled with the tunable, bright emission from a single site, renders this class of materials promising as optically-addressable qubits and other quantum applications.

The presence of SPE depends on the size and chirality of the tube, as well as the chemical structure of the dopant, and so understanding the fundamental properties of these materials provides a potential for material design. The  $sp^3$  defect can be incorporated into the SWCNT by a diazonium reaction, <sup>12</sup> with a degree of control over the attached functional group and

defect density. This synthetic flexibility allows for tuning of its PL energy, emission intensity, excited state lifetime, and exciton-phonon coupling.  $^{13-15}$  While the SWCNT consists of only carbon  $sp^2$  bonds, with delocalized  $\pi$  states responsible for low-energy excitations, the defect introduces an  $sp^3$  bond and a localized defect potential. The trapping energy associated with this state is  $\sim 100$  meV, much larger than  $k_BT$ , which leads to room temperature SPE,  $^{10}$  and the weak electron-phonon interactions in the tube explain the high purity of the emitted emitted exciton. Improving SPE yield requires maximizing the trapping potential while maintaining the exciton coherence, and thus, understanding the nature of the exciton.

Experimentally, the presence of an  $sp^3$  defect results in a bright red-shifted PL peak, which has exhibited SPE properties.  $^{8,10}$  This is illustrated for the case of (6,5) SWCNTs doped with a nitrophenyl (NPL)-functional group in Fig.1a. Here, a low energy peak,  $E_{11}^*$ , is introduced via the defect at  $\sim 1.1$  eV, 0.17 eV lower than the pristine SWCNT peak,  $E_{11}$ , which is expected to originate from the  $\pi$  orbitals of the SWCNT. For some doped SWCNTs, the symmetry breaking induced by the dopant is proposed as the source of  $E_{11}^*$ .  $^{16-20}$  Here, the dopant does not introduce a trap state or unpaired spins into the electronic structure of the tube but causes the degenerate  $\pi$  states to split in energy, resulting in one lowered and one higher energy transition. However, when unpaired spins and trap states are introduced, there may be a more complex nature to the  $E_{11}^*$  transition. We recently demonstrated with a combination of modeling and electron paramagnetic resonance (EPR) measurements that within the (6,5) SWCNT, sp<sup>3</sup> defects can result in a single unpaired spin near the sp<sup>3</sup> site, introducing an electronic state within the bandgap of the SWCNT and a magnetic moment into the system. The physical origin of  $E_{11}^*$  in this case is unknown and may be due to correlation of spin and optical excitations.

In this letter, we simulate the optical absorption and emission spectrum of NPL-doped (6,5) SWCNT using a combination of many-body perturbation theory within the GW/BSE approximation and constrained density functional theory (CDFT). CDFT describes the structural relaxation in the excited-state (Stokes shift), while GW/BSE allows us to an-

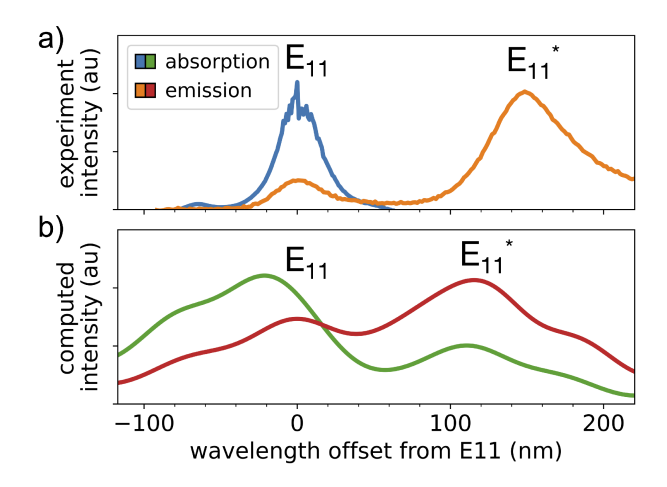


Figure 1: a) Measured and b) simulated absorption and PL spectra for pristine and nitrophenyl-doped (6,5) SWCNT. The peaks  $E_{11}$  and  $E_{11}^*$  in the simulated absorption correspond to Peaks 4 and 3, respectively, in Figure 3b).

alyze the nature of the low-energy excitons. We determine that while the defect introduces low-energy excited states into the optical absorption spectrum of the SWCNT, the  $E_{11}^*$  peak can be attributed to a predominantly band-like transition of a symmetry broken nature. We demonstrate that the competing spin channels lead to a new nature of the exciton when compared with the pristine material.

Figure 1b shows the predicted optical absorption and PL spectra of NPL-(6,5) SWCNT within the experimental energy window. Both absorption and emission show two main peaks within this window, which we label  $E_{11}$  and  $E_{11}^*$  in the Figure. The prediction is in contrast to measured optical absorption where the  $E_{11}^*$  is not present, likely due to the low defect density in experiment. The predicted absorption peaks occur at 1050 nm (1.18 eV) and 1200 nm (1.03 eV), while predictedemission peaks are located at 1075 nm (1.15 eV) and 1190 nm (1.04 eV), in reasonable agreement with the measurement at 975 nm (1.27 eV) and 1150 nm (1.08 eV). The 30 meV red-shift of the  $E_{11}$  peak from absorption to emission is due to atomic relaxation upon electronic excitation (Stokes shift). The relatively large excited state reorganization compared with the pristine tube ( $\sim 9$  meV) is due to symmetry breaking at the  $sp^3$  site.  $^{21,22}$  As seen from both theory and experiment, in absorption, the relative intensity of  $E_{11}$  is higher than  $E_{11}^*$ , while this trend is reversed in PL. This can be

explained from Kasha's rule: an exciton relaxes from the higher energy degenerate excited states to the lowest energy state resulting in redistribution of the oscillator strengths towards the lower energy transition.

There is a notable discrepancy between theory and experiment in the peak energy and broadening. This can be explained by the relatively large defect concentration in our simulation (250  $\mu$ m<sup>-1</sup>), which is two orders of magnitude larger than experiment ( $\sim 5-40~\mu$ m<sup>-123</sup>). As discussed below, we expect that overdoping the SWCNT leads to a a large energy splitting within the bands due to symmetry breaking, with a blue-shifted E<sub>11</sub> and red-shifted E<sub>11</sub> transition. This hypothesis corroborated by experimental results which show that a larger energy splitting between E<sub>11</sub> and E<sub>11</sub> peaks is observed with increasing defect density <sup>24,25</sup> along with broadening of E<sub>11</sub> and E<sub>11</sub> peaks; upon overdoping, those peaks are no longer well-resolved. <sup>13,15</sup> We expect that, for calculations at low defect concentration, less pronounced defect-induced symmetry breaking will result in E<sub>11</sub> and E<sub>11</sub> excited state energy closer to experiment and diminished intensity of peaks below 1 eV. Nevertheless, at this defect concentration, we capture the peak energies within 0.1 eV of experiment, and intensity reversal of the peaks, providing evidence that the predicted peaks are those of the experiment.

To better understand the nature of these two peaks adn the impact of the defect, we plot the bandstructure and optical absorption spectrum for pristine and NPL-doped SWCNT in Figures 2 and 3.

For the pristine (6,5) SWCNT, the mirror symmetry present in the underlying graphitic structure with two nearly-equivalent carbon atoms leads to a two-fold degeneracy within the  $\pi$ -type near-gap states (Figure 2a). We predict a band gap between occupied and unoccupied states of 2.09 eV. This is larger by 1.12 eV when compared with DFT-LDA previously reported by us<sup>26</sup> because of the more accurate description of electron correlation effects within many-body perturbation theory. These near-gap states lead to  $\pi$ - $\pi$  transitions with strong exciton binding of 1.0 eV. There is a single bright transition at 1.09 eV, red-shifted from the experimentally measured lowest energy absorption peak at 1.27 eV. The excitation

is a linear combination of two nearly- degenerate valence bands (VB1, VB2) and conduction bands (CB1, CB2) and similar to the (8,0) SWCNT, only the second excited-state is bright due to symmetry. Since the lowest energy optical transition is a linear combination of these four delocalized  $\pi$ -states, the exciton wave function is delocalized spanning over two unit cells as shown in the density plot Figure 2c. Assuming a Gaussian distributed wave function form, we obtain the standard deviation of the exciton density to be 1.2 nm, with a full-width half maximum of the distribution of 2.87 nm.

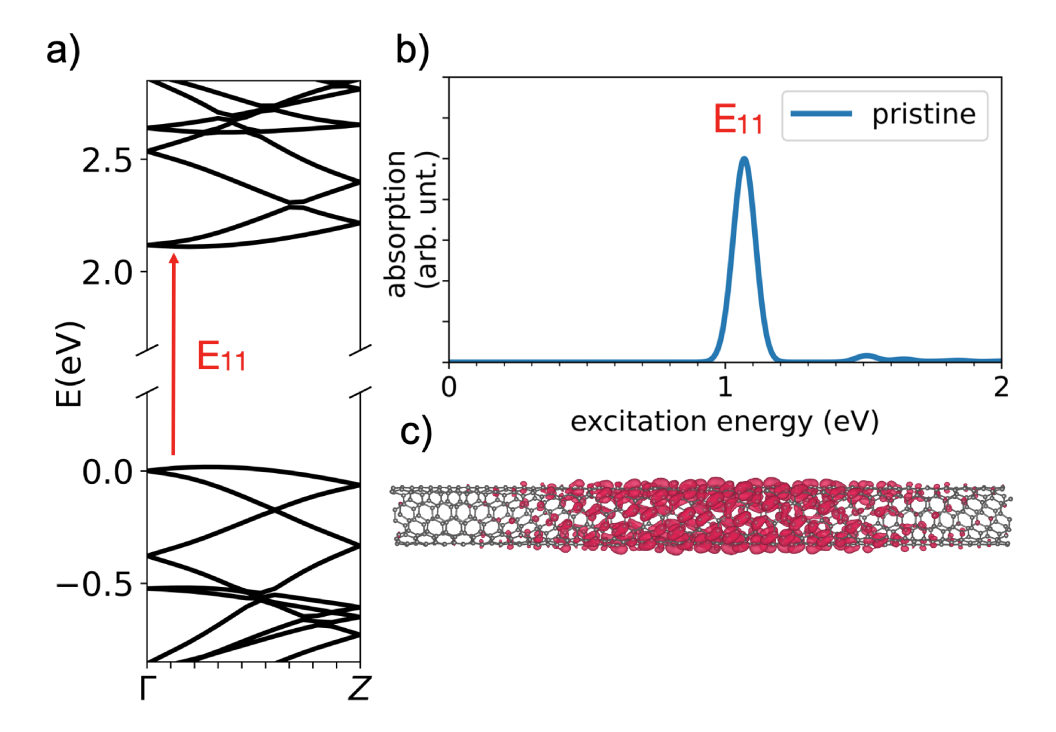


Figure 2: The bandstructure and excitonic properties of pristine (6,5) SWCNT. a) The quasiparticle band structure with the transition character of the lowest energy exciton indicated. b) The optical absorption spectrum with the lowest energy bright transition labeled E11. c) A representation of the delocalized exciton wave function plot associated with the E11 transition.

The defect modifies the quasiparticle band structure of the tube in two main ways as shown in Fig. 3a. First, a singly occupied mid-gap defect band with exchange splitting of 1.1 eV is introduced. The occupied spin up (unoccupied spin down) defect band is 0.30 eV (1.41 eV) from the pristine-like valence band maximum. Second, the degeneracy at pristine-like band edges (valence bands VB1, VB2 and conduction bands CB1, CB2) is broken. The

degeneracy splitting in the valence band is 80 meV, while in the conduction band the splitting is 40 meV. Both these features contribute to new transitions in the absorption spectrum as highlighted with the color-coded arrows in the bandstructure.

There are multiple spin-conserving transitions that are traversed, resulting in four peaks at 0.70 eV, 0.88 eV, 1.04 eV, and 1.18 eV (labeled transition 1-4 in Figure 3b), instead of the single bright peak at 1.1 eV in the pristine tube. We note that Peaks 3 and 4 correspond to the  $E_{11}$  and  $E_{11}^*$  transitions for Figure 1. The lowest energy exciton binding energy is 0.9 eV, similar to that in the pristine tube. Peaks 1 and 2 are mainly of defect-to-band and band-to-defect character, Peak 4 is mainly of band-to-band character, and Peak 3 is a combination of both. While Peak 4 is of band-to-band character, it is blue-shifted from the pristine peak at 1.09 eV. This is likely due to quantum confinement of the exciton at high defect concentrations as discussed later.

Because the defect state is singly occupied with a significant spin exchange splitting between spin channels, there is unequal participation of spin-conserving transitions in Peaks 1-4. While the lowest excitation energy required for a valance bands to the unoccupied defect band excitation is 1.4 eV, the energy required to excite the defect band to the conduction bands is 1.8 eV resulting in larger contributions from the  $\beta$  spin channel for excitations with defect character. This asymmetry is strongest in Peak 1, and decreases but is present up to energies of < 1.3 eV. Based on the exciton wavefunction plot, spin up (red) and down (blue), shown in Figure 3c), Peak 3 (E<sub>11</sub>\*) is composed of localized spin down and delocalized spin up transitions with the spin down transitions having a stronger weight in the wavefunction while Peak 4 (E<sub>11</sub>) is a combination of localized and delocalized transition for both up and down spin with smaller difference between spin channels. Qualitatively, excitons associated with Peak 4 are more delocalized than those in Peak 3. Delocalization of the exciton around the hole position is characteristic of the pristine tube lowest energy transition. Peak 3 has more defect character mixed in and therefore is more localized compared with Peak 4.

To quantify the localization of excited-states that result in Peaks 1-4, we fit the exciton

wavefunction of all transitions associated with a given peak to a Gaussian function and quantify delocalization from the standard deviation of the function. In general, the standard deviation is ~12 nm for delocalized excitons (similar to the pristine distribution of 13 nm) and 1.5 nm for localized excitons with significant defect character. For Peaks 1 and 2, fitting the exciton states to a Gaussian results in a standard deviation range of 0.2-0.3 nm. For Peaks 3 and 4, fitting results in a standard deviation ranges of 0.2-0.3 nm for localized states and 1.1-1.4 nm for delocalized states. The majority of states contributing to Peak 3 are more localized while those for Peak 4 are more delocalized, indicating that the exciton goes from defect-localized to pristine-like as the energy of the excitation is increased.

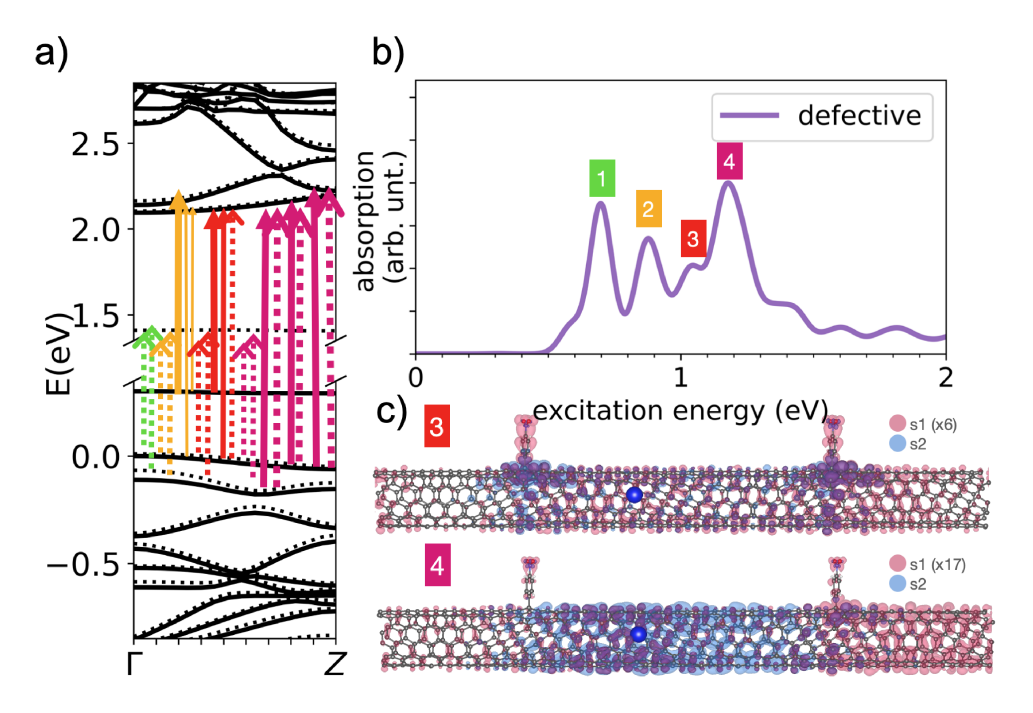


Figure 3: Excitonic and optical properties of nitrophenyl-defective (6,5) SWCNT. a) quasiparticle band structure showing a mid-gap defect band and a band gap of 2.1 eV. Solid (dotted) line corresponds to spin up (down) bands. The defect band is only singly occupied. b) optical absorption spectrum with the lowest bright energy transitions labeled with the transition character depicted in a). c) localized, delocalized exciton wave function plot associated with the transition 3, 4. For transition 3, contribution from spin up (down) is shown in red (blue). Blue dot corresponds to the chosen hole position, which was determined to be a high probability location.

We considering exciton localization associated with photoluminescence peaks  $E_{11}$  and  $E_{11}^*$ ,

where the structure of the doped tube relaxes upon a  $\pi=\pi$  transition. Upon excited state geometry relaxation, excitons associated with both  $E_{11}$  and  $E_{11}^*$  become more delocalized (see Table1). To understand the relative delocalization, we define the parameter  $\eta$ , defined as the fraction of  $\pi-\pi$ -like transitions to the overall transition averaged over all excitonic states contributing to each peak (see SI Section SX for details). An  $\eta$  value of 1 indicate the peak is fully  $\pi-\pi$ -like and an  $\eta$  value of 0 fully defect-centered. For Peak 3, upon absorption  $\eta=0.38$ , indicating that the majority of the states making up the peak are localized defect-centered transitions, while at emission  $\eta=0.59$ , a 55% increase in delocalization with the majority of states delocalized in nature. Peak 4 displays a delocalized nature for both absorption and emission, with  $\eta=0.70$  and 0.75, respectively, with a 7% increase in delocalization upon emission. Upon structural relaxation in the excited state, each peak is more delocalized with a 12% increase across both peaks, indicating that the structure rearranges such that transitions are more pristine,  $\pi$ -like excitations.

Table 1: The fraction of delocalization within the exciton wavefunctions averaged over all states  $(\eta)$  that make up Peaks 3 and 4 for the absorption and emission spectra. The respective peak energy range is shown.

	Peak	energy range (eV)	$\eta$
absorption	3	0.99-1.08	0.38
emission	3	0.97 - 1.10	0.59
absorption	4	1.13-1.31	0.70
emission	4	1.13-1.29	0.75
absorption	3-4	0.99 - 1.31	0.58
emission	3-4	0.97 - 1.29	0.65

We note that the excitation energy, oscillator strength, and spin-dependence of these low-energy transitions depend on defect density. Increase of defect concentration leads to quantum confinement of the exciton wavefunction as well as enhanced symmetry breaking due to the defect when compared to experiment. There is one singly occupied defect band for two valence and conduction band-edge states, resulting in overestimation of participation from the defect band. We can see evidence of the defect-defect interactions because the localized exciton wavefunction has significant weight on multiple defects (indicating exciton band

formation). Additionally, a confinement potential associated with the presence of multiple defects localizes the pristine-like exciton and shifts excitation energy up. At large defect density, defect-localized states contribute more significantly to the absorption process compared with transitions from the pristine tube  $\pi$ -states resulting in multiple defect-centered orbitals in the theory, which may explain the lack of observed at low concentrations experimentally in the region of Peaks 1 and 2. This conclusion is consistent with the unresolved absorption spectrum reported for high  $sp^3$ -defect density. <sup>13,15</sup> Furthermore, oscillator strength redistribution to defect transitions below 1 eV may be responsible for experimentally observed darkening of the  $E_{11}$  and  $E_{11}^*$  transitions upon overdoping. We anticipate that experimentally, high concentration of defects that are nonuniformly spaced will result in a range of dark states below 1 eV in contrast to well-resolved peaks 1,2 predicted in our periodic calculations.

Table 2: Excited state energy and Stokes shift calculated from CDFT at LDA level. The pristine transition is a transition from VB1-CB1 while for defective SWCNT multiple transitions are considered (as labeled).

System	Pristine	Defect VB1-CB1	Defect VB1-DF	Defect VB2-DF	Defect DF-CB1
E (eV)	1.04	1.04	0.50	0.55	0.80
Stoke's shift (meV)	13.1	29.3	40.0	29.3	31.9

Lastly, we consider whether electron-phonon interactions increase upon addition of the defect by calculating the Stokes shift and atomic rearrangement upon excited-state transitions associated with Peaks 1-4 of Figure 3. We compute the excited-state energy relaxation associated with band-like and defect-to-band/band-to-defect transitions within constrained DFT. We expect that both exciton localization due to the presence of the defect and breaking of degeneracy will result in increased electron-phonon coupling and larger Stokes shift. The computed Stokes shifts for these transitions are shown in Table 2. For the valence to conduction transition, the presence of the defect increases the Stokes shift from 13 meV to 29 meV, presumably due to the symmetry breaking. When the transition includes the mid-gap defect state, the Stokes shift ranges from 30 meV to 40 meV, indicating a stronger electron-phonon

coupling due to the localized defect state. This strong electron-phonon coupling leads to redistribution of oscillator strength from the bright  $E_{11}$  state to a lower energy band-edge transition  $E_{11*}$  state as noted in intensity reversal reported.

In summary, we investigated the origin of the red-shifted emission peak,  $E_{11^*}$ , in  $sp^3$ -defective (6,5) SWCNT with an unpaired electron near the defect site. The introduction of the  $sp^3$ -defect introduces local geometric perturbation near the  $sp^3$  defect site breaking the  $sp^2$  symmetry. The consequences of this symmetry breaking is two fold: 1) introduction of a spin-split defect band; and 2) increased electron-phonon coupling. Both contribute to funneling of oscillator strength from the  $E_{11}^*$  to  $E_{11}$  state. Analysis of the bandstructure and excitonic properties of the doped-SWCNT indicate that the spin-split defect band leads to asymmetry between the contribution of the two spin channels, with one spin channel leading to localized excitons, while the other leads to delocalized pristine-like excitons. This finding indicates that this material, with a single unpaired electron and possible spin-selective optical transitions is promising for an optical addressable spin qubit. Future studies of defect-density dependence and spin selectivity are needed to understand the impact of the defect state.

### Acknowledgments

We acknowledge financial support from the U.S. Department of Energy (DOE), Office of Science, Basic Energy Sciences under Award No. DE-SC0023402. X.L. acknowledges support from the National Science Foundation DMR Program under award no. DMR-1905990. Work performed at the Center for Nanoscale Materials, a U.S. Department of Energy Office of Science User Facility, was supported by the U.S. DOE, Office of Basic Energy Sciences, under Contract No. DE-AC02-06CH11357. We would like to acknowledge computational resources from Advanced Cyberinfrastructure Coordination Ecosystem: Services Support (ACCESS), which is supported by the NSF grant number ACI-1548562, the National Energy Research Scientific Computing Center (NERSC), a DOE Office of Science User Facility sup-ported

by the Office of Science of the U.S. Department of Energy under Contract No. DE-AC02-05CH11231, and Boston University's Research Computing Services.

## Computational Details

The ground-state electronic structure of the SWCNT system and its spin properties was simulated by spin-polarized DFT with LDA functional within the VASP package  $^{27-30}$  with core electrons and nuclei described by the projector-augmented wave method (PAW).  $^{31,32}$  Scalar relativistic effects were included in the PAW. The SWCNT system was placed in an orthorhombic unit cell with 10 Åof vacuum added around the aperiodic directions. In VASP, we used a plane wave cutoff energy was 400 eV with a  $\Gamma$ -centered k-point mesh of 1x1x2. All structures were optimized such that forces between atoms were smaller than 0.01 eV/Å. The resulting geometry optimized lattice vectors were a=20 Å(32.5 Å), b=20 Å(20 Å), c=40.45 Å(40.45 Å) for the pristine (defective) system. The geometry of the system was relaxed within LDA, with the periodic c-vector in good agreement with previous tight-binding  $^{33,34}$  and DFT  $^{35,36}$  calculations. The magnetic moment was initialized at a high value (5  $\mu$ B) and allowed to optimize during the self-consistent process, resulting in a net magnetic moment of 1  $\mu$ B, in agreement with our previous computational and experimental studies.  $^{37}$ 

Quasiparticle and optical properties were described by the  $G_0W_0$ @LDA approximation <sup>38,39</sup> and Bethe-Salpether equation (BSE) <sup>40,41</sup> within the BerkeleyGW package. <sup>42</sup> MBPT has been shown to accurately describe defect energetics within a variety of materials. <sup>43</sup> Initial wavefunctions were generated from the Quantum Espresso package <sup>44</sup> with Troullier-Martins norm-conserving pseudopotentials <sup>45</sup> using a psudopotential cutoff of 60 Rydberg. To simulate structural relaxation of the SWCNT system in the excited state, geometries were relaxed with fixed occupation corresponding to a neutral excitation (CDFT). The CDFT-BSE method has been applied successfully to understand the PL of other defective semiconducting SWCNTs. <sup>20,21</sup> The number of unoccupied states that build the dielectric function and self-

energy operator were 20.0, 22.65 eV above the valence band maximum with a  $1 \times 1 \times 2$  k-point mesh. The BSE was solved with a 16 valence and 16 conduction states. The quasiparticle energies were interpolated onto a  $1 \times 1 \times 16$  k-point mesh. To avoid spurious interactions between aperiodic directions, the Coulomb potential was truncated along the a and b lattice vectors at half of the unit cell length<sup>46</sup>

# **Experimental Details**

(6,5) SWCNT raw material (Sigma-Aldrich SG65i, ¿95%) was dispersed in 1 wt % aqueous sodium deoxycholate (DOC) solution via tip sonication at an output power of 5 W/mL (Sonics, model GEX 750) in an ice water bath for 1 hour. The sonicated suspension was subsequently ultracentrifuged at 16000 rpm for 2 hours at ambient temperature (Beckman-Coulter Avanti J-E high-speed centrifuge SW-32Ti swing-bucket rotor) to remove large bundled SWCNTs as well as impurities. Single-chirality (6,5) SWCNTs was sorted through two-step phase separation method from the supernatant as reported previously. 47 and then transferred into 1 wt% sodium dodecyl sulfate (SDS) solution through pressure filtration (Millipore Amicon stirred cell with ultracel 100 kDa cellulose membrane). 48 The samples were then diluted to an optical density of 0.16 at the E11 absorption peak of (6,5)-SWCNTs by 1 wt% SDS solution. 0.425 mg of 4-nitrobenzenediazonium tetrafluoroborate (C6H4N3O2 · BF4, Sigma-Aldrich, 97%) was dissolved in 1 mL of acetonitrile (ACN, Sigma-Aldrich, 99.8%). This stock solution was diluted by a factor of 75 using DI water and then 150 μL of the diluted solution was added into 10 mL of diluted CNT solution. The mixture was kept in dark and stirred under 300 rpm for 26 hours. The degree of functionalization was monitored by photoluminescence spectrum using a Nanolog spectrofluorometer (Horiba Jobin Yvon) equipped with a liquid-N2-cooled InGaAs detector.

### References

- (1) Laird, E. A.; Kuemmeth, F.; Steele, G. A.; Grove-Rasmussen, K.; Nygård, J.; Flensberg, K.; Kouwenhoven, L. P. Quantum transport in carbon nanotubes. Reviews of Modern Physics 2015, 87, 703–764.
- (2) Akizuki, N.; Aota, S.; Mouri, S.; Matsuda, K.; Miyauchi, Y. Efficient near-infrared up-conversion photoluminescence in carbon nanotubes. *Nature Communications* 2015, 6, 8920.
- (3) Abudulimu, A.; Spaeth, F.; Namal, I.; Hertel, T.; Lüer, L. Chirality Specific Triplet Exciton Dynamics in Highly Enriched (6,5) and (7,5) Carbon Nanotube Networks. *The Journal of Physical Chemistry C* **2016**, *120*, 19778–19784.
- (4) Spataru, C. D.; Ismail-Beigi, S.; Capaz, R. B.; Louie, S. G. Theory and Ab Initio Calculation of Radiative Lifetime of Excitons in Semiconducting Carbon Nanotubes. *Physical Review Letters* 2005, 95, 247402.
- (5) Capaz, R. B.; Spataru, C. D.; Ismail-Beigi, S.; Louie, S. G. Diameter and chirality dependence of exciton properties in carbon nanotubes. *Physical Review B* 2006, 74, 121401.
- (6) Kilina, S.; Ramirez, J.; Tretiak, S. Brightening of the Lowest Exciton in Carbon Nanotubes via Chemical Functionalization. *Nano Letters* **2012**, *12*, 2306–2312.
- (7) Scholes, G. D.; Tretiak, S.; McDonald, T. J.; Metzger, W. K.; Engtrakul, C.; Rumbles, G.; Heben, M. J. Low-Lying Exciton States Determine the Photophysics of Semiconducting Single Wall Carbon Nanotubes. *The Journal of Physical Chemistry C* 2007, 111, 11139–11149.
- (8) Ma, X.; Hartmann, N. F.; Baldwin, J. K. S.; Doorn, S. K.; Htoon, H. Room-temperature

- single-photon generation from solitary dopants of carbon nanotubes. *Nature Nanotech-nology* **2015**, *10*, 671–675.
- (9) Ma, X.; Adamska, L.; Yamaguchi, H.; Yalcin, S. E.; Tretiak, S.; Doorn, S. K.; Htoon, H. Electronic Structure and Chemical Nature of Oxygen Dopant States in Carbon Nanotubes. ACS Nano 2014, 8, 10782–10789.
- (10) He, X.; Hartmann, N. F.; Ma, X.; Kim, Y.; Ihly, R.; Blackburn, J. L.; Gao, W.; Kono, J.; Yomogida, Y.; Hirano, A.; Tanaka, T.; Kataura, H.; Htoon, H.; Doorn, S. K. Tunable room-temperature single-photon emission at telecom wavelengths from sp3 defects in carbon nanotubes. *Nature Photonics* 2017, 11, 577–582.
- (11) Chen, J.-s.; Trerayapiwat, K. J.; Sun, L.; Krzyaniak, M. D.; Wasielewski, M. R.; Rajh, T.; Sharifzadeh, S.; Ma, X. Long-lived electronic spin qubits in single-walled carbon nanotubes. *Nature Communications* 2023, 14, 848.
- (12) Strano, M. S. Electronic Structure Control of Single-Walled Carbon Nanotube Functionalization. *Science* **2003**, *301*, 1519–1522.
- (13) Piao, Y.; Meany, B.; Powell, L. R.; Valley, N.; Kwon, H.; Schatz, G. C.; Wang, Y. Brightening of carbon nanotube photoluminescence through the incorporation of sp3 defects. *Nature Chemistry* 2013, 5, 840–845.
- (14) Gifford, B. J.; He, X.; Kim, M.; Kwon, H.; Saha, A.; Sifain, A. E.; Wang, Y.; Htoon, H.; Kilina, S.; Doorn, S. K.; Tretiak, S. Optical Effects of Divalent Functionalization of Carbon Nanotubes. *Chemistry of Materials* 2019, 31, 6950–6961.
- (15) Sykes, M. E.; Kim, M.; Wu, X.; Wiederrecht, G. P.; Peng, L.; Wang, Y.; Gosztola, D. J.; Ma, X. Ultrafast Exciton Trapping at sp 3 Quantum Defects in Carbon Nanotubes. ACS Nano 2019, 13, 13264–13270.

- (16) Kim, Y.; Goupalov, S. V.; Weight, B. M.; Gifford, B. J.; He, X.; Saha, A.; Kim, M.; Ao, G.; Wang, Y.; Zheng, M.; Tretiak, S.; Doorn, S. K.; Htoon, H. Hidden Fine Structure of Quantum Defects Revealed by Single Carbon Nanotube Magneto-Photoluminescence. ACS Nano 2020, 14, 3451–3460.
- (17) Gifford, B. J.; Kilina, S.; Htoon, H.; Doorn, S. K.; Tretiak, S. Exciton Localization and Optical Emission in Aryl-Functionalized Carbon Nanotubes. *Journal of Physical Chemistry C* 2018, 122, 1828–1838.
- (18) Saha, A.; Gifford, B. J.; He, X.; Ao, G.; Zheng, M.; Kataura, H.; Htoon, H.; Kilina, S.; Tretiak, S.; Doorn, S. K. Narrow-band single-photon emission through selective aryl functionalization of zigzag carbon nanotubes. *Nature Chemistry* **2018**, *10*, 1089–1095.
- (19) Gifford, B. J.; Kilina, S.; Htoon, H.; Doorn, S. K.; Tretiak, S. Controlling Defect-State Photophysics in Covalently Functionalized Single-Walled Carbon Nanotubes. *Accounts* of Chemical Research 2020, 53, 1791–1801.
- (20) Mu, J.; Ma, Y.; Liu, H.; Zhang, T.; Zhuo, S. Optical properties of semiconducting zigzag carbon nanotubes with and without defects. *Journal of Chemical Physics* **2019**, 150.
- (21) Ma, Y.; Rohlfing, M.; Gali, A. Excited states of the negatively charged nitrogen-vacancy color center in diamond. *Physical Review B Condensed Matter and Materials Physics* **2010**, *81*, 1–4.
- (22) Kim, M.; Adamska, L.; Hartmann, N. F.; Kwon, H.; Liu, J.; Velizhanin, K. A.; Piao, Y.; Powell, L. R.; Meany, B.; Doorn, S. K.; Tretiak, S.; Wang, Y. Fluorescent Carbon Nanotube Defects Manifest Substantial Vibrational Reorganization. *The Journal of Physical Chemistry C* 2016, 120, 11268–11276.
- (23) Sebastian, F. L.; Zorn, N. F.; Settele, S.; Lindenthal, S.; Berger, F. J.; Bendel, C.; Li, H.; Flavel, B. S.; Zaumseil, J. Absolute Quantification of sp3Defects in Semiconducting

- Single-Wall Carbon Nanotubes by Raman Spectroscopy. *Journal of Physical Chemistry Letters* **2022**, *13*, 3542–3548.
- (24) Mu, J.; Ma, Y.; Yin, H.; Liu, C.; Rohlfing, M. Photoluminescence of single-walled carbon nanotubes: The role of stokes shift and impurity levels. *Physical Review Letters* **2013**, *111*, 1–5.
- (25) Ghosh, S.; Bachilo, S. M.; Simonette, R. A.; Beckingham, K. M.; Weisman, R. B. Oxygen doping modifies near-infrared band gaps in fluorescent single-walled carbon nanotubes. *Science* **2010**, *330*, 1656–1659.
- (26) Trerayapiwat, K. J.; Lohmann, S.; Ma, X.; Sharifzadeh, S. Tuning spin-orbit coupling in (6,5) single-walled carbon nanotube doped with sp 3 defects. *Journal of Applied Physics* **2021**, *129*, 014309.
- (27) Kresse, G.; Furthmüller, J. Efficiency of ab-initio total energy calculations for metals and semiconductors using a plane-wave basis set. *Computational Materials Science* **1996**, *6*, 15–50.
- (28) Kresse, G.; Hafner, J. Ab initio molecular-dynamics simulation of the liquid-metal-amorphous-semiconductor transition in germanium. *Physical Review B* **1994**, 49, 14251–14269.
- (29) Kresse, G.; Hafner, J. Ab initio molecular dynamics for liquid metals. *Physical Review B* **1993**, 47, 558–561.
- (30) Kresse, G.; Furthmüller, J. Efficient iterative schemes for ab initio total-energy calculations using a plane-wave basis set. *Physical Review B* **1996**, *54*, 11169–11186.
- (31) Blöchl, P. E. Projector augmented-wave method. *Physical Review B* **1994**, *50*, 17953–17979.

- (32) Kresse, G.; Joubert, D. From ultrasoft pseudopotentials to the projector augmentedwave method. *Physical Review B* **1999**, *59*, 1758–1775.
- (33) Yang, L.; Anantram, M. P.; Han, J.; Lu, J. P. Band-gap change of carbon nanotubes: Effect of small uniaxial and torsional strain. *Physical Review B* **1999**, *60*, 13874–13878.
- (34) Gyungseon, S.; Youngki, Y.; K, F. J.; Jing, G.; Akira, M.; Diego, K.; Gengchiau, L.; Gerhard, K.; Mark, L.; Ibrahim, S. A. CNTbands. 2019; https://nanohub.org/resources/cntbands-ext.
- (35) Correa, J. D.; Orellana, W. Light-harvesting efficiency of a (6,5) carbon nanotube functionalized with a free-base tetraphenylporphyrin: Density functional theory calculations. *Journal of Applied Physics* **2013**, *113*, 174305.
- (36) Orellana, W. Strong π-π Interaction of Porphyrins on (6,5) Carbon Nanotubes with Full Surface Coverage: Ab-initio Calculations. *Applied Physics Letters* **2014**, *105*, 023110.
- (37) Lohmann, S.-H.; Trerayapiwat, K. J.; Niklas, J.; Poluektov, O. G.; Sharifzadeh, S.; Ma, X. sp 3 -Functionalization of Single-Walled Carbon Nanotubes Creates Localized Spins. ACS Nano 2020, 14, 17675–17682.
- (38) Ceperley, D. M.; Alder, B. J. Ground State of the Electron Gas by a Stochastic Method. *Physical Review Letters* **1980**, *45*, 566–569.
- (39) Perdew, J. P.; Zunger, A. Self-interaction correction to density-functional approximations for many-electron systems. *Physical Review B* **1981**, *23*, 5048–5079.
- (40) Onida, G.; Reining, L.; Rubio, A. Electronic excitations: density-functional versus many-body Green's-function approaches. *Reviews of Modern Physics* **2002**, *74*, 601–659.
- (41) Rohlfing, M.; Louie, S. G. Electron-hole excitations and optical spectra from first principles. *Physical Review B* **2000**, *62*, 4927–4944.

- (42) Deslippe, J.; Samsonidze, G.; Strubbe, D. A.; Jain, M.; Cohen, M. L.; Louie, S. G. BerkeleyGW: A massively parallel computer package for the calculation of the quasi-particle and optical properties of materials and nanostructures. Computer Physics Communications 2012, 183, 1269–1289.
- (43) Lewis, D. K.; Sharifzadeh, S. Modeling Excited States of Point Defects in Materials from Many-Body Perturbation Theory. *ACS Materials Letters* **2021**, *3*, 862–874.
- (44) Giannozzi, P. et al. QUANTUM ESPRESSO: a modular and open-source software project for quantum simulations of materials. *Journal of Physics: Condensed Matter* **2009**, *21*, 395502.
- (45) Troullier, N.; Martins, J. L. Efficient pseudopotentials for plane-wave calculations. *Physical Review B* **1991**, *43*, 1993–2006.
- (46) Ismail-Beigi, S. Truncation of periodic image interactions for confined systems. *Physical Review B Condensed Matter and Materials Physics* **2006**, *73*, 1–4.
- (47) Subbaiyan, N. K.; Cambré, S.; Parra-Vasquez, A. N. G.; Hároz, E. H.; Doorn, S. K.; Duque, J. G. Role of Surfactants and Salt in Aqueous Two-Phase Separation of Carbon Nanotubes toward Simple Chirality Isolation. ACS Nano 2014, 8, 1619–1628.
- (48) Chen, J.-S.; Dasgupta, A.; Morrow, D. J.; Emmanuele, R.; Marks, T. J.; Hersam, M. C.; Ma, X. Room Temperature Lasing from Semiconducting Single-Walled Carbon Nanotubes. ACS Nano 2022, 16, 16776–16783.